



Modeling of methanol decomposition on Pt/CeO₂/ZrO₂ catalyst in a packed bed microreactor



Andrej Pohar^{a,*}, Darko Belavič^b, Gregor Dolanc^c, Stanko Hočevar^a

^a Laboratory of Catalysis and Chemical Reaction Engineering, National Institute of Chemistry, Hajdrihova 19, SI-1000 Ljubljana, Slovenia

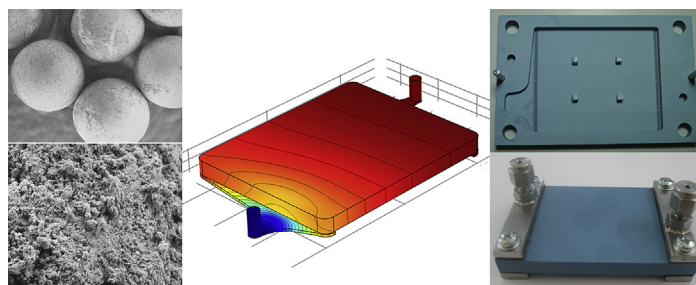
^b HIPOT-RR d.o.o., Šentpeter 18, SI-8222 Otočec, Slovenia

^c Department of Systems and Control, Jožef Stefan Institute, Jamova 39, SI-1000 Ljubljana, Slovenia

HIGHLIGHTS

- Methanol decomposition on Pt/CeO₂/ZrO₂ inside a packed-bed microreactor was studied.
- A 1D and a full 3D computational fluid dynamics model were developed and evaluated.
- Further optimization of the LTCC microreactor structure can be achieved.
- Pt/CeO₂ catalyst is highly stable and is unaffected by surface poisoning.

GRAPHICAL ABSTRACT



ARTICLE INFO

Article history:

Received 22 October 2013

Accepted 11 January 2014

Available online 18 January 2014

Keywords:

Microreactor

Methanol decomposition

Ceria catalyst

Modeling

ABSTRACT

Methanol decomposition on Pt/CeO₂/ZrO₂ catalyst is studied inside a packed bed microreactor in the temperature range of 300–380 °C. The microreactor is fabricated using low-temperature co-fired ceramic (LTCC) technology, which is well suited for the production of relatively complex three-dimensional structures. It is packed with 2 wt% Pt–CeO₂ catalyst, which is deposited onto ZrO₂ spherical particles. A 1D mathematical model, which incorporates diffusion, convection and mass transfer through the boundary layer to the catalyst particles, as well as a 3D computational fluid dynamics model, are developed to describe the methanol decomposition process inside the packed bed. The microreactor exhibits reliable operation and no catalyst deactivation was observed during three months of experimentation. A comparison between the 1D mathematical model and the 3D model, considering the full 3D geometry of the microreactor is made and the differences between the models are identified and evaluated.

© 2014 Elsevier B.V. All rights reserved.

1. Introduction

Hydrogen has been recognized as one of the more important energy carriers of the future [1]. Its suitability for miniaturized portable fuel cell power sources is mainly because of its high energy density on a mass basis and microchemical systems are especially suitable for portable fuel cells due to efficient heat and mass

transfer characteristics and compact size [2]. The use of fuel cells for generating electricity is showing promise since they are an environmentally friendly, clean and efficient energy source [3].

It has been demonstrated that microreactors offer superior operation as opposed to conventional fixed-bed catalytic reactors in terms of methanol conversion and hydrogen selectivity, most likely due to the advantage of being able to achieve optimal process conditions for the desired chemical transformation, and by taking advantage of the large surface area [4]. The methanol decomposition reaction is endothermic and is favored at high temperatures [5], which necessitates efficient heat transfer characteristics of the

* Corresponding author. Tel.: +386 1 4760283; fax: +386 1 4760300.
E-mail address: andrej.pohar@ki.si (A. Pohar).

system. For microreactor fabrication, low temperature co-fired ceramic (LTCC) technology is a promising technique for producing relatively complex three-dimensional multilayer structures, by the bonding of several ceramic layers [6]. The integration of sensors and actuators with microelectromechanical systems (MEMS) technology has been reported [7].

For hydrogen storage, methanol is the most attractive hydrogen fuel carrier due to its high hydrogen to carbon ratio. With the exception of formic acid, methanol is the easiest hydrocarbon to reform and liquid methanol can readily be produced from biomass, unlike gasoline or diesel fuel [8]. It is also much safer and more convenient to distribute and store hydrogen chemically bonded in liquid form than as a pure compound for long-distance transportation or through gas pipelines [9]. Moreover, methanol is sulfur-free and the absence of carbon–carbon bonds reduces the risk of coking [1].

Among the processes to recover hydrogen from methanol the most frequently used is methanol steam reforming, which gives the highest concentration of hydrogen and the lowest concentration of carbon monoxide in the reformat stream. However, it requires an overstoichiometric concentration of water in the feed, which may cause degradation of phosphoric acid doped polybenzimidazole high-temperature PEM membrane in the fuel cell. In order to avoid this undesired influence, one can use a methanol decomposition based fuel processor [10].

Pt/CeO₂ catalyst has been reported to be among the best for the methanol decomposition reaction [11]. The addition of CeO₂ stabilizes catalyst operation by preventing carbon decomposition on the surface, which leads to enhancements in hydrogen selectivity and yield [12]. Pt and Pd based catalysts promoted with ceria have been found to be significantly more active than catalysts, which are not promoted. Furthermore, the presence of ceria decreases the temperature required for complete conversion, which was explained as being most likely due to the ability of ceria to stabilize small Pt crystallites [8].

In this work, methanol decomposition inside a LTCC microreactor packed with Pt/CeO₂/ZrO₂ catalyst was studied. The kinetic parameters were evaluated and a comparison was made between a simplified 1D model and a 3D model, which took into account the full 3D geometry of the microreactor.

2. Materials and methods

2.1. Catalyst preparation

Mesoporous ceria support having a BET specific surface area of 132 m² g^{−1} was synthesized by using a hard template method with KIT-6 silica [13]. The 2 wt% Pt–CeO₂ catalyst precursor was prepared by wet impregnation of CeO₂ with a solution of dihydrogen hexachloroplatinate hydrate (>99.9%, Sigma–Aldrich, St. Louis, USA) in ethanol. The resulting material was dried overnight at 60 °C in ambient air. A suspension of the prepared catalyst precursor was further deposited with a method of vacuum evaporation onto 350 μm ZrO₂ spherical beads. The ZrO₂ beads, coated with the catalyst precursor, were then dried at 125 °C for 2 h and subsequently calcinated at 550 °C for 3 h in a flow of air to obtain a core–shell catalyst. Before catalyst testing, it was reduced in situ at 220 °C for 4 h in a flow of 5 vol% H₂ in Ar. Scanning electron microscope (SEM) images of the catalyst were made. The catalyst BET surface area was measured with a MicroMeritics ASAP2010 instrument.

2.2. Microreactor design

The microreactor was fabricated with LTCC technology, as described elsewhere [14]. Single ceramic layers were manufactured, laminated together and fired in one step at a low firing

temperature of approximately 850 °C. The microreactor consisted of inflow and outflow ports for fluidic connections (ϕ 2.6 mm), 4 mounting ports (ϕ 4.5 mm), and a service port for the insertion of the catalytic spheres (Fig. 1a). A grate at the entrance and exit of the catalytic bed with 76 ducts, each with a dimension of 1 × 0.15 mm, was fabricated for the entrapment of the catalytic particles and for allowing the passage of gas. The catalytic beads were poured into the microreactor through the service hole, which was finally filled with fiberglass and closed with graphite sealing tape and Swagelok connection ports, which were fitted at the inlet and outlet (Fig. 1b). The use of spherical catalyst particles for the packed bed is advantageous, since closed areas inaccessible to the flow and stagnant zones are less likely to exist.

The catalytic bed had the dimensions 33.8 × 3 × 41.4 mm (width × depth × length), which yielded approximately 4.2 cm³ reaction chamber space. The total microreactor size was 63.8 × 6 × 41.8 × mm.

2.3. Process set-up

The process set-up is illustrated on Fig. 2. Laboratory syringe pumps (TSE Systems, Chesterfield, USA) with 5 ml glass syringes were used for methanol dosage (of analytical grade; Sigma–Aldrich, St. Louis, USA). An evaporator, consisting of a 1/16" stainless steel coil capillary with an integrated heater, was used for the production of vapor methanol. The evaporator was kept at a constant temperature between 120 and 150 °C, depending on the flow rate. Vaporized methanol was subsequently fed into the microreactor, which was positioned inside an electric heater with a quartz sand bath, thermostated at the operational temperature. Due to the endothermic reaction, sufficient heating was provided and the preset microreactor temperature was kept constant within $\pm 1^\circ$ in the temperature range of 300–380 °C. The gas from the microreactor outlet was directly connected to a gas chromatograph for analysis. Nitrogen gas was preheated and added to the gaseous reaction stream through a mass flow controller and was used as the internal standard. Experimentation was conducted at liquid methanol flow rates of 2–70 μL min^{−1}, which corresponds to volume hourly space velocities of 400–13,700 h^{−1}. The volume hourly space velocity is defined as the total volumetric flow rate to the microreactor at standard temperature and pressure, divided by the volume of the catalyst in the microreactor.

2.4. Gas chromatographic analysis

Vapor composition from the microreactor exit was analyzed with an Agilent 7890A gas chromatograph (Agilent Technologies, Santa Clara, USA). Two capillary columns: HP-PLOT-Q (30 m × 0.53 mm × 40 μm) and HP-PLOT-5A (30 m × 0.53 mm × 50 μm) with a TCD detector at 200 °C, equipped with molecular sieves, were used, with helium as the carrier gas. Oven temperature was kept at 140 °C for 12 min after which the temperature was decreased at the rate of 20 °C min^{−1} 100 °C. The retention times of methanol, hydrogen, nitrogen and carbon monoxide were identified at 5.1, 9.2, 15.1, 15.8, and 17.1 min, respectively. Quantitative analysis of the reactants and products was enabled after the calibration with standard gas mixtures.

3. Modeling

3.1. One-dimensional model

In the packed bed microreactor, methanol is decomposed to carbon monoxide and hydrogen (CH₃OH → CO + 2H₂). The decomposition reaction is endothermic with $\Delta H_{298} = 90.7$ kJ mol^{−1}

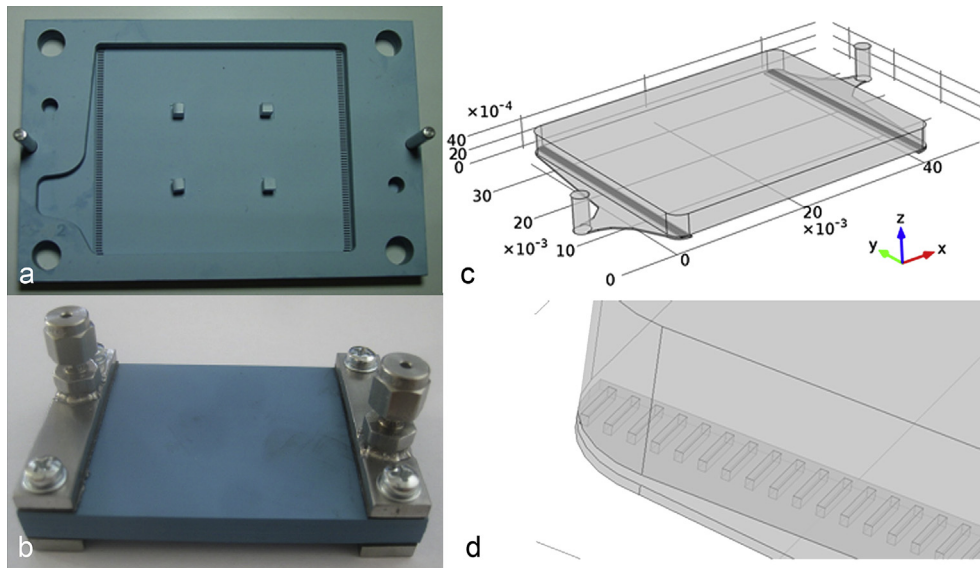
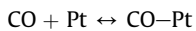
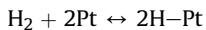
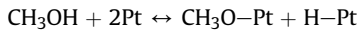


Fig. 1. (a) The bottom layer of the LTCC microreactor displaying the catalytic bed with a grate at the inlet and outlet. (b) The assembled LTCC microreactor with metal fittings. (c) The model of the microreactor; units in meters. (d) A close-up of the grate connecting the inlet channel with the reaction chamber.

[8]. The adsorption equilibrium of the reacting species can be written [11]:

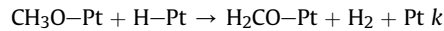


The equilibrium constants of methanol (K_m), hydrogen (K_h) and carbon monoxide (K_c) are therefore:

$$K_m = \frac{\theta_{\text{CH}_3\text{O}}\theta_{\text{H}}}{P_{\text{MeOH}}\theta_v^2} \quad K_h = \frac{\theta_{\text{H}}^2}{P_{\text{H}_2}\theta_v^2} \quad K_c = \frac{\theta_{\text{CO}}}{P_{\text{CO}}\theta_v} \quad (1)$$

where $\theta_{\text{CH}_3\text{O}}, \theta_{\text{H}}, \theta_{\text{CO}}$ are the concentrations of the species bound to the catalyst and θ_v is the concentration of the vacant sites. P_i is the partial pressure of each species.

The dominant dissociation pathway of methanol involves the cleavage of the O–H bond [15], while the abstraction of the hydrogen atom from the methyl group was found to be the rate determining step of methanol decomposition [11,16]:



where k is the kinetic constant. The derived rate equation of the limiting step, considering $\theta_{\text{CH}_3\text{O}} + \theta_{\text{H}} + \theta_{\text{CO}} + \theta_v = 1$, is:

$$r = \frac{kK_m P_{\text{MeOH}}}{\left(1 + K_m K_h^{-1/2} P_{\text{MeOH}} P_{\text{H}_2}^{-1/2} + K_h^{-1/2} P_{\text{H}_2}^{-1/2} + K_c P_{\text{CO}}\right)^2} \quad (2)$$

Due to the small inner reactor dimensions and short diffusion pathways, the operation of the miniaturized reactor was described with a one-dimensional isothermal model with x as the length coordinate. Diffusion, convection and mass transfer through the boundary layer to the catalyst particles were included in the mass balance of bulk flow. For low values of the Reynolds number ($Re < 1$), the dispersion coefficient is equal to the molecular diffusion coefficient [17].

$$\frac{d}{dx} \left(D_i \frac{dc_i}{dx} \right) - \frac{d(v c_i)}{dx} - \frac{(1-\varepsilon)}{\varepsilon} k_{c,i} a (c_i - c_{\text{cat},i}) = 0 \quad (3)$$

Index i represents methanol, nitrogen, hydrogen and carbon monoxide. The Danckwerts boundary conditions are as follows:

$$-D_i \frac{dc_i}{dx} \Big|_{x=0^+} = v c_i|_{0^-} - v c_i|_{0^+} \quad x = 0$$

$$dc_i/dx = 0 \quad x \rightarrow \infty$$

where D_i is the diffusion coefficient of each species, c_i is the bulk concentration, $c_{\text{cat},i}$ is the concentration at the catalyst surface, v is the interstitial velocity, and a is the surface area per void volume. The mass balance at the catalyst surface is:

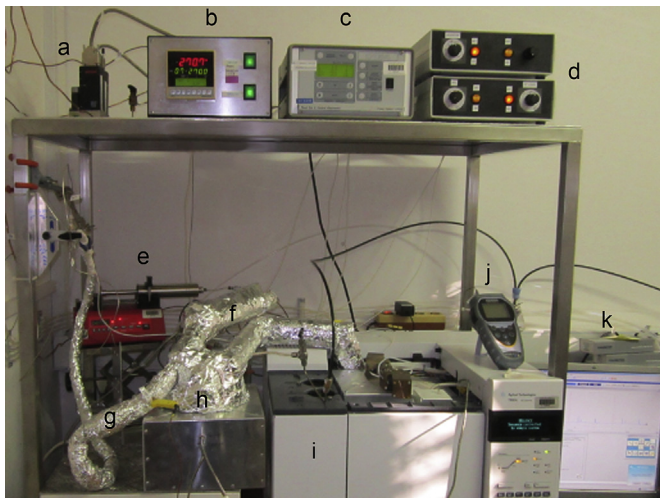


Fig. 2. The experimental set-up; (a) mass flow controllers (MFCs), (b) heater for the microreactor, (c) the control unit for MFCs, (d) the control unit for additional heaters (evaporator, nitrogen inlet, inlet to the gas chromatograph), (e) laboratory syringe pump, (f) evaporator, (g) nitrogen inlet, (h) thermostated microreactor inside the heater, (i) gas chromatograph, (j) temperature indicator, (k) computer analysis software.

$$k_{c,i}a(c_{cat,i} - c_i) = \nu_i r \quad (4)$$

where ν_i is the coefficient of stoichiometry and $k_{c,i}$ is the mass transfer coefficient. Vapor viscosities of the non-polar gases involved in the reaction were predicted with the Stiel and Thodos correlation [18] from their critical temperatures ($T_{c,i}$) and pressures ($P_{c,i}$):

$$\eta_i = 4.6 \times 10^{-4} N_i \frac{M_i^{1/2} P_{c,i}^{2/3}}{T_{c,i}^{1/6}} \quad (5)$$

where M_i is the molar mass in g mol⁻¹ and

$$N_i = 3.4 \times 10^{-4} T_{r,i}^{0.94} \quad T_r \leq 1.5$$

$$N_i = 1.778 \times (4.58 T_{r,i} - 1.67)^{0.625} \quad T_r > 1.5$$

$$T_{r,i} = T/T_{c,i} \quad (6)$$

Viscosities of polar gases were calculated from the method of Chung et al. [19], which accounts for the molecular shape and the polarity of polar gases:

$$\eta_i = 40.785 \frac{F_{c,i}(M_i T)^{1/2}}{V_{c,i}^{2/3} \Omega_{v,i}} \quad (7)$$

in which case the viscosity is in μP , the molar mass is in g mol⁻¹, $V_{c,i}$ is the critical volume in cm³ mol⁻¹, and $\Omega_{v,i}$ is the viscosity collision integral, defined as [20]:

$$\Omega_{v,i} = 1.16145 (T_i^*)^{-0.14874} + 0.52487 \exp(-0.77320 T_i^*) + 2.16178 \exp(-2.43787 T_i^*)$$

$$T_i^* = 1.2593 T_{r,i} \quad (8)$$

Eq. 8 is valid in the range $0.3 \leq T_i^* \leq 100$, with an average deviation of only 0.064% [21]. The factor $F_{c,i}$ accounts for the molecular shapes and polarities of dilute gases:

$$F_{c,i} = 1 - 0.2756 \omega_i + 0.059035 \mu_{r,i}^4 + \kappa_i$$

$$\kappa_i = 0.0682 + 4.704 N_{OH,i} / M_i$$

$$\mu_{r,i} = 131.3 \frac{\mu_i}{(V_{c,i} T_{c,i})^{1/2}} \quad (9)$$

where ω_i is the acentric factor, κ_i is a correction for highly polar substances, $\mu_{r,i}$ is a dimensionless dipole moment, μ_i is the dipole moment in debyes, and $N_{OH,i}$ is the number of -OH groups.

The viscosity of the gaseous mixture is a function of pressure and composition and varies along the microreactor length. It was calculated via the following expression, which is accurate at low pressures, at each segment of the microreactor:

$$\eta = \frac{\sum x_i \eta_i (M_i)^{1/2}}{\sum x_i (M_i)^{1/2}} \quad (10)$$

where x_i is the mole fraction of component i with viscosity η_i and molar mass M_i and is calculated from:

$$x_i = \frac{c_i}{\sum c_i} \quad (11)$$

Similarly, the gas mixture density was calculated considering ideal gas behavior:

$$\rho_{\text{mix}} = \frac{P}{RT} \sum M_i x_i \quad (12)$$

where P is the pressure, R is the gas constant, and T is the temperature. The pressure drop for spherical packing in a packed bed reactor was calculated with the Ergun equation:

$$\frac{dP}{dx} = -\frac{G}{\rho D_p} \left(\frac{1-\varepsilon}{\varepsilon^3} \right) \left(\frac{150(1-\varepsilon)\eta}{D_p} + 1.75G \right) \quad (13)$$

which takes into account the characteristics of the packing (void fraction ε , particle diameter D_p), the characteristics of fluid properties (viscosity η , density ρ), and the characteristics of the operating parameters (mass velocity G). The pressure was calculated from the outlet of the microchannel (at 1 atm) to the inlet and iterated along with the equations of state. The packing characteristics were considered invariant with respect to reactor length and the operation was assumed to be steady-state and isothermal.

The mass transfer coefficients ($k_{c,i}$) were calculated from the correlation for the Sherwood numbers (Sh_i) through an expression proposed by Comiti et al. [22] at each longitudinal position of the channel:

$$Sh_i = 3.66 + 0.101 \left(1 + \frac{\pi(1-\varepsilon)}{4\varepsilon} (\tau - 1) \right) \times \left(1 + \frac{\varepsilon}{\tau^2} Sc_i^{1/3} \exp \left(-\frac{11-\varepsilon}{3\varepsilon} \sqrt{\tau Y X_e^{1/8}} \right) \right) \times X_e^{11/48} Sc_i^{1/3}$$

$$k_{c,i} = \frac{Sh_i D_i}{D_p} \quad (14)$$

The equation is valid for laminar and turbulent flow at $0.03 < Re < 10^5$. τ represents tortuosity, which is the ratio of the actual length of the flow path to the straight-line distance between the ends of the flow path, and is therefore $\pi/2$ for spherical particles. Y is the particle aspect ratio, defined in the direction normal to the flow, and is equal to 1 for spheres. Sc_i is the dimensionless Schmidt number ($Sc_i = \eta/\rho D_i$) and X_e is the dimensionless wall energetic criterion, which can be calculated for porous media:

$$X_e = 64 Re^2 \left(1 + 1.21 \times 10^{-2} Re \right) \quad (15)$$

The Reynolds number, for fluid flow in a packed bed of approximately spherical particles, is:

$$Re = \frac{\rho V_s D_p}{\eta(1-\varepsilon)} \quad (16)$$

where V_s is the superficial velocity of the flow.

The diffusion coefficients in multicomponent gas mixtures of the species under consideration were calculated from the binary diffusion coefficients through the following relation [23]:

$$D_A = \frac{1 - x_A}{\frac{x_B}{D_{AB}} + \frac{x_C}{D_{AC}} + \frac{x_D}{D_{AD}} + \dots} \quad (17)$$

where D_A is the effective diffusion coefficient of gas A with respect to the total gas mixture, while D_{AB} , D_{AC} , etc. are the binary diffusion coefficients.

The diffusion coefficients of binary gas mixtures were calculated with a diffusion volume correlation method, developed by Fuller et al. [24]:

$$D_{AB} = \frac{10^{-8} T^{1.75} (1/M_A + 1/M_B)^{1/2}}{P \left(\left(\sum_A v_j \right)^{1/8} + \left(\sum_B v_j \right)^{1/8} \right)^2} \quad (18)$$

in which case D_{AB} is in the units of $\text{cm}^2 \text{s}^{-1}$, P is the pressure in atm, and v_j is a special atomic diffusion volume parameter, provided in the reference for each constitutive atom of the gas.

The velocity increase of the gaseous mixture due to the reaction was calculated considering ideal gas behavior. Mass fractions (w_i) and partial pressures (P_i) were calculated from molar fractions:

$$w_i = \frac{x_i M_i}{\sum x_i M_i} \quad (19)$$

$$P_i = x_i P \quad (20)$$

The vapor properties were evaluated at every position in the microreactor and were corrected with the pressure field in the iterative solving process. Finite differences were used for the numerical discretization with the inclusion of a pseudo time step for the treatment of the second derivative in the mass balance equations. The discretization of the computational domain was refined until no grid dependence was observed. A $60 \times 30,000$ (length \times time) discretization was used with the initial conditions the same as the inlet boundary conditions. The solution was iterated until it converged to steady state with a desired accuracy level. Matlab was used for performing the calculations.

3.2. Three-dimensional CFD model

Additionally, a 3D finite element steady-state model was developed. The microchannel geometry was modeled, meshed, and solved with COMSOL Multiphysics. The model consisted of an inlet and outlet channel, and a catalytic reaction chamber (packed bed with porous media flow), where the reaction took place. The pressure and the velocity were continuous over the interface between the free and porous domain. Gravitational effects were neglected. Continuity and momentum balance equations (Navier–Stokes equations) were used for modeling the compressible laminar flow:

$$\nabla(\rho \mathbf{u}) = 0 \quad (21)$$

$$\rho(\mathbf{u} \cdot \nabla) \mathbf{u} = -\nabla P + \nabla \cdot \left(\mu \left(\nabla \mathbf{u} + (\nabla \mathbf{u})^T \right) \right) + \left(-\frac{2\mu}{3} \nabla \cdot \mathbf{u} \right) \quad (22)$$

where \mathbf{u} is the velocity vector. The Brinkman equation was used for modeling flow through a porous matrix:

$$\frac{\rho}{\varepsilon} \left((\mathbf{u} \cdot \nabla) \frac{\mathbf{u}}{\varepsilon} \right) = -\nabla P + \nabla \cdot \left(\frac{1}{\varepsilon} \left(\mu \left(\nabla \mathbf{u} + (\nabla \mathbf{u})^T \right) \right) + \left(-\frac{2\mu}{3} \nabla \cdot \mathbf{u} \right) \right) - \left(\frac{\mu}{\kappa_p} \right) \mathbf{u} \quad (23)$$

where κ_p is the permeability of the porous medium.

The Maxwell–Stefan diffusion model was used for the description of mass transfer:

$$\nabla \cdot \mathbf{j}_i + \rho(\mathbf{u} \cdot \nabla) \omega_i = r_i \quad (24)$$

$$\mathbf{j}_i = - \left(\rho \omega_i \sum_k D_{ik} \mathbf{d}_k \right) \quad (25)$$

$$\mathbf{d}_k = \nabla x_k + \frac{1}{P} ((x_k - \omega_k) \nabla P) \quad (26)$$

where \tilde{D}_{ik} are the multicomponent Fick diffusivities and \mathbf{d}_k is the diffusional driving force acting on species k . The kinetic expression is presented in Eq. (2). Mass transfer limitations were not included due to the information obtained from the results of the 1D model. The boundary conditions are the Danckwerts boundary conditions:

Inlet:

$$j_i|_{y=0^+} = v_{in} \rho \omega_i|_{y=0^-} - v_{in} \rho \omega_i|_{y=0^+} \quad (27)$$

v_{in} is the inlet normal velocity calculated from the flow rate and the inlet area (A_{in}).

Outlet:

$$j_i = 0; P = 1 \text{ atm} \quad (28)$$

The no flux and no-slip boundary conditions were used on the remaining boundaries. The permeability of the packed bed (κ) was calculated with the correlation published by Rumpf and Gupte [25]:

$$\kappa_p = \frac{\varepsilon^{5.5}}{5.6} D_p^2 \quad (29)$$

Several grid sizes were tested to ensure that the results were grid insensitive and 573,511 tetrahedral elements were finally used. The convergence criteria for the normalized residuals for each variable were restricted to less than 10^{-6} .

4. Results and discussion

The reaction chamber was filled with approximately 1.16×10^5 Pt/CeO₂/ZrO₂ catalyst spherical particles with an average diameter (D_p) of 350 μm and a total mass of 12.5 g. The total amount of the catalyst on the particles, obtained by weighting coated and uncoated catalyst particles, is 83 mg. The calculated void volume (ε) of the chamber is 0.38 and the permeability (κ) is $1.07 \times 10^{-10} \text{ m}^2$ (from Eq. (29)). BET analysis determined a specific surface area of 0.2 $\text{m}^2 \text{g}^{-1}$. Fig. 3 presents the SEM image of the coated core–shell catalyst. The average thickness of the shell is approximately 5 μm . Energy-dispersive X-ray spectroscopy (EDS) performed on the catalyst particles identified 38.7 wt% O, 34.4 wt% Zr, 25.1 wt% Ce, and 1.73 wt% Pt.

Numerical simulations show that the rate expression (Eq. (2)) in steady state can be reduced to:

$$r = k_D K_{\text{Me}} K_{\text{CO}}^{-2} P_{\text{Me}} P_{\text{CO}}^{-2} \quad (30)$$

The natural logarithms of $k_D K_{\text{Me}} K_{\text{CO}}^{-2}$ values, obtained with regression analysis at each experimental temperature (300, 317, 340, 355, 380 $^\circ\text{C}$), in dependency to reciprocal temperature, give a linear correlation (Fig. 4, Table 1).

The results at 380 $^\circ\text{C}$ and a flow rate of 10 $\mu\text{L min}^{-1}$ liquid methanol with 10 wt% N₂ show an increase of the mean velocity in the cross-section of the reaction chamber (yz plane) from 0.095 to 0.11 m s^{-1} (15.8%) due to the change in gas density, which is a consequence of the reaction stoichiometry, producing 3 mol of the products from 1 mol of the reactant. The pressure drop inside the microreactor was mostly linear with a pressure difference of 125 Pa. The velocity distribution across the chamber cross-section is mainly uniform, apart from some variation at the entrance and exit of the chamber, due to the bottom positioned inlet and outlet grate.

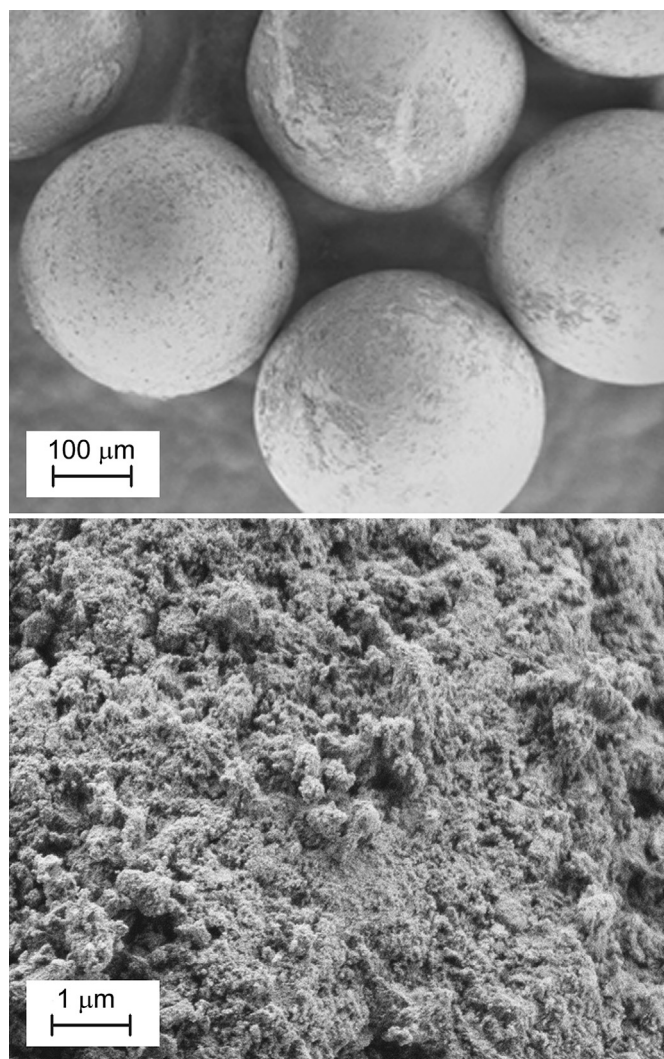


Fig. 3. SEM image of the ZrO₂ spherical beads (core) with 2 wt% Pt/CeO₂ catalyst shell.

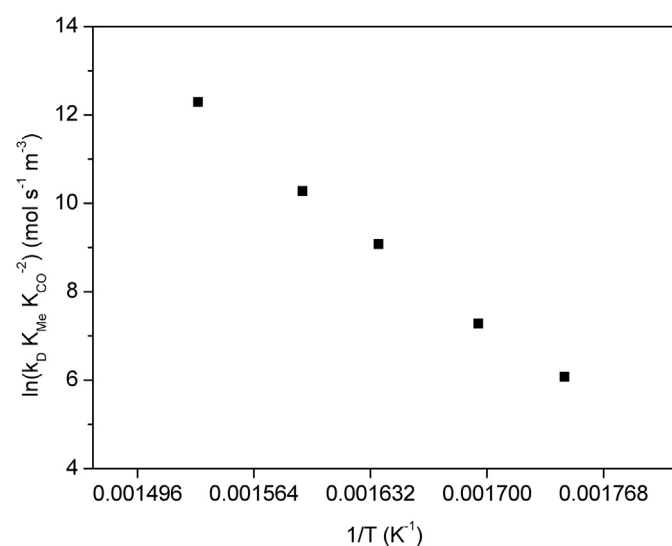


Fig. 4. The natural logarithm of the kinetic parameters as a function of reciprocal temperature.

Table 1

The values of the kinetic expression, which consists of the kinetic and equilibrium constants, obtained by regression analysis.

T (°C)	$k_D K_{Me} K_{CO}^{-2}$ (mol s ⁻¹ m ⁻³ Pa)
300	4.4×10^2
317	1.5×10^3
338	8.7×10^3
355	2.9×10^4
380	2.2×10^5

Fig. 5 presents the velocity magnitude on 3 yz and 1 xy planes. The xy plane is positioned 0.2 mm above the inlet and outlet grate. The color range is set to 0–0.02 m s⁻¹ for a better view of the velocity magnitude inside the reaction chamber. On the first yz plane at the top of the chamber a lower velocity at the entrance can be seen; this is similar at the exit (not shown for a better view of the exit grate). The highest velocity 1.237 m s⁻¹ is located inside the outlet grate. The red lines present the fluid flow streamlines, which portray an evenly distributed flow.

Fig. 6 presents the comparison between the velocity magnitudes of the 1D model and the 3D model. For the 3D model, the velocity magnitude on 3 lines at the middle of the reaction chamber, running along the length of the reactor, at different depths were chosen (3D centerline – through the middle of the depth, 3D bottom 1/4 – at the bottom quarter of the chamber, and 3D top 1/4 – at the top quarter of the chamber). The higher velocities at the entrance and exit can be observed in the bottom 1/4 of the chamber due to the bottom positioned inlet and outlet grates with a smaller cross section area. In contrast, the velocity at the top 1/4 of the chamber, which is located on the other side of the inlet and outlet grate, is lower at the entrance and exit of the reaction chamber.

Fig. 7 presents the methanol mass fraction distribution. A surface plot is presented due to the small variance of methanol mass fraction in the direction of depth. The inlet mass fraction is 0.9 methanol and 0.1 N₂, which was used as the standard for the gas chromatography analysis. The catalyst particles are only present inside the reaction chamber, whereas a substantial lowering of the methanol mass fraction (and an increase of CO and H₂) can be observed inside the inlet channel, due to the fast diffusion process, which works to level out the concentration difference. The mass fraction of methanol entering the reaction chamber is already reduced to around 0.4. The mass fraction graphs of CO and H₂ are presented in Supplementary.

The mass fractions of the species constituting the gas inside the reaction chamber are presented on Fig. 8. The 3D model values are the calculated average values across the chamber cross-section (yz plane). The mass fraction of methanol is lower at the entrance to the reaction chamber due to the fast diffusion, and is accurately described by the inlet Danckwerts boundary condition. Similarly, the mass fractions of H₂ and CO at the entrance are already 0.06 and 0.38. The 3D results predict a lower conversion compared to the 1D model which is expected, since they describe the deviation from ideal, 1D operation, due to localized velocity and concentration variations. A 20% increase of the value of the kinetic expression is required for the 3D model to overlay the 1D model solution. Modeling results from the 1D model also revealed that there was no mass transfer resistance due to fast molecular diffusion to the catalyst surface.

Fig. 9 shows the mass fractions in dependence of the residence times. The results of the model were obtained by setting the flow rates of liquid methanol between 8 and 1500 μL min⁻¹, at 380 °C, and with 10 wt% N₂. Together with the added nitrogen gas, this corresponds to inlet gas mixture velocities of 0.2–37.3 mL min⁻¹ and a maximum residence time of 8 s. The residence time τ was

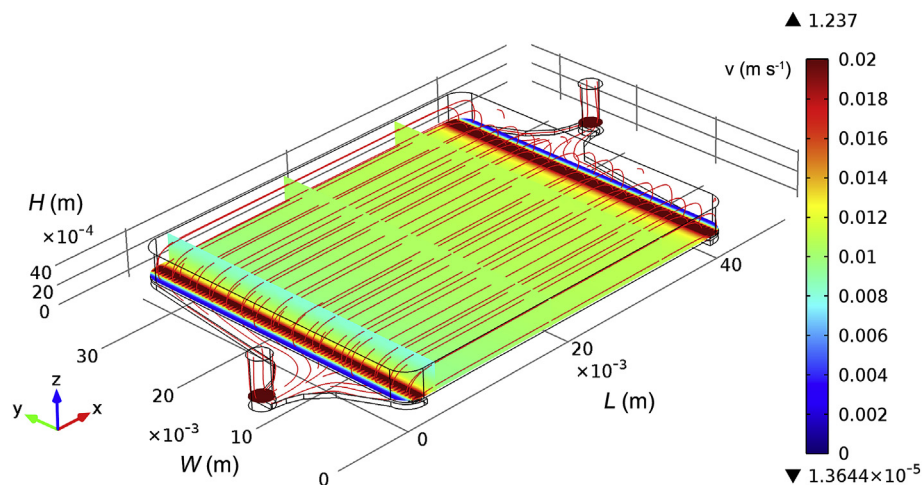


Fig. 5. The velocity magnitude inside the packed bed microreactor. The color bar is for 0–0.02 m s^{−1}. The red lines on the graph represent the fluid streamlines. (For interpretation of the references to color in this figure legend, the reader is referred to the web version of this article.)

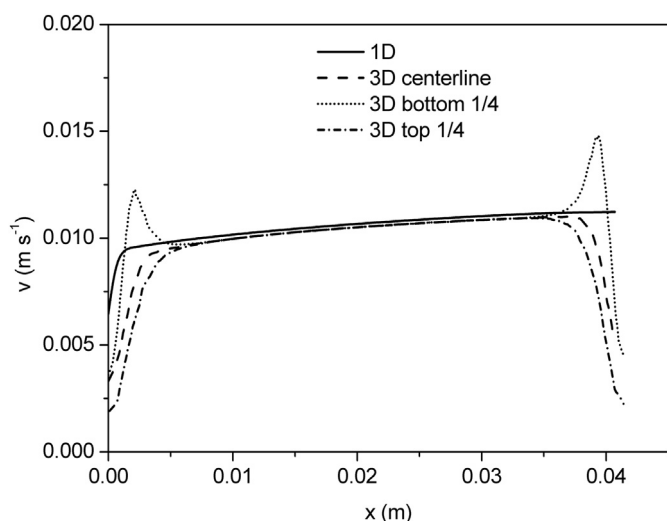


Fig. 6. The velocity magnitude along the length of the microreactor for the 1D model and the 3D model. The velocity magnitude of the 3D model is presented on lines running through the middle of the microreactor along the length at 3 different height positions.

calculated from the void volume of the microreactor and the flow rate. The experimental values were obtained with a liquid methanol flow rate of 10, 40, and 70 $\mu\text{L min}^{-1}$. Gas constitution at the lowest experimental flow rate was 5.10 wt% methanol, 71.6 wt% CO, 9.25 wt% H₂, and 14.05 wt% N₂. With the acquired kinetic constants, a good agreement was found between the modeling results and the experimental data. At the experimental flow rate of 10 $\mu\text{L min}^{-1}$, 94% methanol conversion was achieved.

The catalyst exhibited no deactivation after three months of intensive experimentation and EDS analysis did not detect any carbon deposited. Matolín et al. [26] found that with Pt/ceria catalysts, a complete removal of carbon-containing intermediates occurs above 500 K. The effect was explained by the reaction of the intermediates with oxygen, provided by reverse spillover from ceria.

5. Conclusions

A packed bed microreactor, fabricated with LTCC technology, is used for studying methanol decomposition. With the microchannel design the velocity distribution achieved inside the packed bed is almost homogenous. 2 wt% Pt–CeO₂ catalyst is a very selective and active methanol decomposition catalyst. The catalyst exhibits

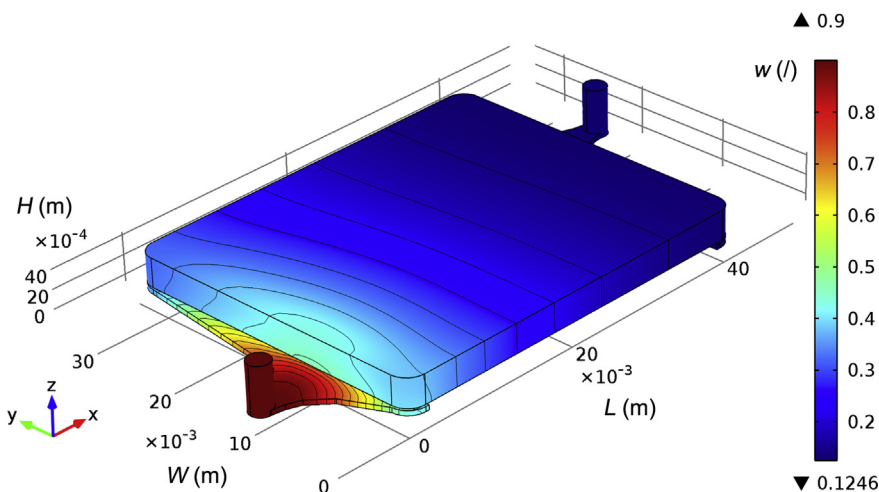


Fig. 7. Methanol mass fraction at 380 °C and the liquid methanol flow rate of 10 $\mu\text{L min}^{-1}$. The geometric values are in meters.

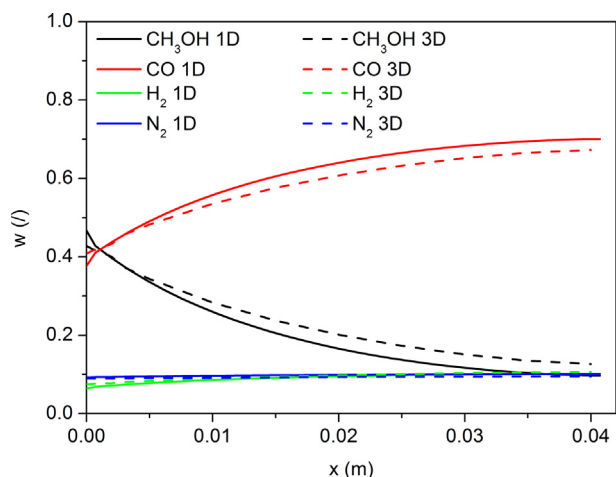


Fig. 8. Modeling results of the mass fractions of the species along the length of the reaction chamber at 380 °C, a liquid methanol flow rate of 10 $\mu\text{L min}^{-1}$ and 10 wt% N_2 . The 3D results are presented as average values across the cross-section (yz plane).

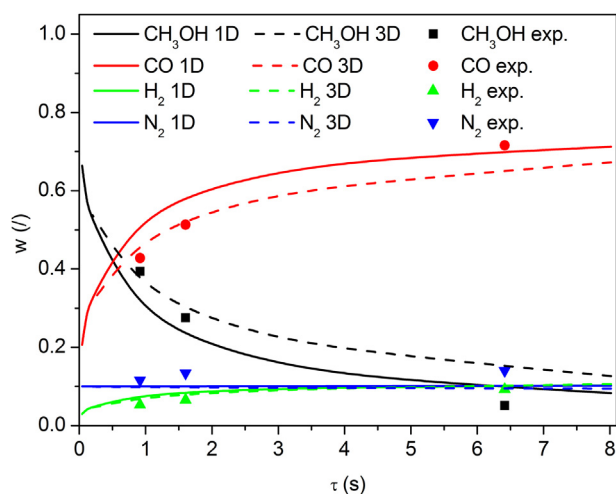


Fig. 9. The mass fractions obtained by the 1D model, 3D model and the experimental results at 380 °C at various residence times.

excellent resistance to surface poisoning by formation of stable carbides, due to the reaction with oxygen, supplied by ceria. Methanation side-reaction does not occur.

An accurate solution is obtained by the 3D model and the deviation of the microreactor from ideal 1D behavior is due to non-ideal flow and concentration distribution. Modeling results show a significant concentration change taking place inside the inlet

channels, even though the reaction only takes place inside the catalytic bed. Optimization of the microreactor geometry would be achieved by positioning the inlet and outlet grates in the flow direction. This way, the gaseous flow would not undergo as many directional changes, which would cause a smaller pressure drop and would provide a uniform velocity distribution. The operation of the reformer would approach ideal behavior, as is described by the 1D model.

Acknowledgments

The research was funded by the European Space Agency (ESA) under PECS Arrangement No 4000103742/11/NL/KML. The provision of financial support for the conduct of the research and preparation of the article by the Slovenian Research Agency (ARRS) (Program P2-0152) is gratefully acknowledged.

Appendix A. Supplementary data

Supplementary data related to this article can be found at <http://dx.doi.org/10.1016/j.jpowsour.2014.01.051>.

References

- [1] A. Kundu, Y.G. Shul, D.H. Kim, in: K.D. Kreuer, T. Van Nguyen, T. Zhao (Eds.), *Advances in Fuel Cells*, Elsevier Science, 2007, pp. 419–472.
- [2] K. Shah, X. Ouyang, R.S. Besser, *Chem. Eng. Technol.* 28 (2005) 303–313.
- [3] Y. Oona, A. Sounai, M. Hori, *J. Power Sources* 241 (2013) 87–93.
- [4] T. Maki, T. Ueyama, K. Mae, *Chem. Eng. Technol.* 28 (2005) 494–500.
- [5] Y. Choi, H.G. Stenger, *J. Power Sources* 142 (2005) 81–91.
- [6] Y. Gao, X. Kong, N. Munroe, K. Jones, *J. Power Sources* 195 (2010) 46–53.
- [7] W.C. Shin, R.S. Besser, *J. Power Sources* 164 (2007) 328–335.
- [8] J.C. Brown, E. Gulari, *Catal. Commun.* 5 (2004) 431–436.
- [9] C.H. Fu, J.C.S. Wu, *Int. J. Hydrogen Energy* 32 (2007) 4830–4839.
- [10] M.S. Wilson, *Int. J. Hydrogen Energy* 34 (2009) 2955–2964.
- [11] S. Imamura, T. Higashihara, Y. Saito, H. Aritani, H. Kanai, Y. Matsumura, N. Tsuda, *Catal. Today* 50 (1999) 369–380.
- [12] A.Y. Kapran, L.M. Alekseenko, S.N. Orlik, *Theor. Exp. Chem.* 45 (2009) 338–342.
- [13] P. Djinić, J. Batista, J. Levec, A. Pintar, *Appl. Catal. A Gen.* 364 (2009) 156–165.
- [14] D. Belavić, M. Hrovat, G. Dolanc, M. Santo–Zarnik, J. Holc, K. Makarović, *Radioengineering* 21 (2012) 195–200.
- [15] P. Tolmásov, A. Gazsi, F. Solymosi, *Appl. Catal. A Gen.* 362 (2009) 58–61.
- [16] O. Tokugawa, Y. Satoh, T. Fukushima, S. Ogasawara, *Sekiyu Gakkaishi* 33 (1990) 173.
- [17] J.M.P.Q. Delgado, *Heat Mass Transfer* 42 (2006) 279–310.
- [18] L.I. Stiel, G. Thodos, *AIChE J.* 7 (1961) 611–615.
- [19] T.H. Chung, M. Ajlan, L.L. Lee, K.E. Starling, *Ind. Eng. Chem. Res.* 27 (1988) 671–679.
- [20] P.D. Neufeld, A.R. Janzen, R.A. Aziz, *J. Chem. Phys.* 57 (1972) 1100–11102.
- [21] B.E. Poling, J.M. Prausnitz, J.P. O'Connell, *The Properties of Gases and Liquids*, McGraw-Hill, New York, 2000.
- [22] J. Comiti, E. Mauret, M. Renaud, *Chem. Eng. Sci.* 55 (2000) 5545–5554.
- [23] D.F. Fairbanks, C.R. Wilke, *Ind. Eng. Chem.* 42 (1950) 471–475.
- [24] E.N. Fuller, P.D. Schettler, J.C. Giddings, *Ind. Eng. Chem.* 58 (1966) 18–27.
- [25] H. Rumpf, A.R. Gupta, *Chem. Ing. Tech.* 43 (1971) 367–375.
- [26] V. Matolín, V. Johánek, M. Skoda, N. Tsud, K.C. Prince, T. Skála, I. Matolínova, *Langmuir* 26 (2010) 13333–13341.